Neutron diffraction observations of interstitial protons in dense ice

Malcolm Guthrie[a,1], Reinhard Boehler[a], Christopher A. Tulk[b], Jamie J. Molaison[b], António M. dos Santos[b], Kuo Li[a], and Russell J. Hemley[a,1]

[a]Geophysical Laboratory, Carnegie Institution of Washington, Washington, DC 20015; and [b]Neutron Sciences Directorate, Oak Ridge National Laboratory, Oak Ridge, TN 37831

Contributed by Russell J. Hemley, May 16, 2013 (sent for review April 22, 2013)

The motif of distinct H_2O molecules in H-bonded networks is believed to persist up to the densest molecular phase of ice. At even higher pressures, where the molecule dissociates, it is generally assumed that the proton remains localized within these same networks. We report neutron-diffraction measurements on D_2O that reveal the location of the D atoms directly up to 52 GPa, a pressure regime not previously accessible to this technique. The data show the onset of a structural change at ∼13 GPa and cannot be described by the conventional network structure of ice VII above ∼26 GPa. Our measurements are consistent with substantial deuteron density in the octahedral, interstitial voids of the oxygen lattice. The observation of this "interstitial" ice VII form provides a framework for understanding the evolution of hydrogen bonding in ice that contrasts with the conventional picture. It may also be a precursor for the superionic phase reported at even higher pressure with important consequences for our understanding of dense matter and planetary interiors.

crystallography | high pressure | water

All of the some 16 phases of crystalline ice documented to date exhibit a tetrahedrally coordinated structure in which each molecule is H-bonded to four neighbors in an extended network. Above ∼2 GPa, the phase diagram contains just two, closely related, molecular phases: orientationally disordered ice VII and its ordered low-temperature analog ice VIII (1). Both phases have body-centered, close-packed oxygen sublattices with cubic and tetragonal symmetry, respectively. Infrared spectroscopy has provided evidence for bond symmetrization in ice VII—meaning covalent and H-bonds become geometrically equivalent, and ice becomes a simple oxide—starting around 60 GPa (2–4). Meanwhile, X-ray diffraction indicates the persistence of a closely body-centered cubic (bcc) oxygen sublattice up to at least 210 GPa (5–9). At the highest pressures, this system has been studied extensively by numerous experimental techniques [including infrared (3–4, 10) and Raman spectroscopy (2, 11), Brillouin scattering (12), and other optical techniques (13) as well as computational theory (e.g., refs. 14–18 and references therein)]. These efforts, spanning almost 50 years, have led to a consensus view that ice VII moves gradually toward a symmetric H-bonded phase (ice X) across a broad pressure range with protons essentially localized between neighboring O-atoms on network sites. However, the positions of the hydrogen nuclei have not been determined directly at pressures sufficient to significantly change the molecular geometry from that found in common ice *Ih* (19). In addition, the nature of the proposed intermediate states between ices VII and X remains uncertain (11, 20), and changes in ices VII and VIII themselves have been suggested by anomalies in X-ray (5, 7, 8, 21, 22) and spectroscopic (12, 22, 23) data beginning as low as 13–14 GPa.

In contrast to other techniques, neutron diffraction can resolve the location of deuterons (D) directly within the lattice of heavy water (D_2O) ice. In situ neutron diffraction at 2.4 GPa of ices VII and VIII (24) first confirmed the interpenetrating H-bond network structures originally proposed to explain X-ray measurements (25). Subsequent higher pressure studies revealed little change in the molecular geometry up to a reported 20 GPa (19) (see comment in *Materials and Methods*). A lack of in situ neutron-diffraction data above this pressure has precluded direct measurement of the D locations on the approach to symmetrization. By developing a supported diamond-anvil cell (S-DAC) (12) and coupling this with the intense radiation flux at the dedicated high-pressure diffraction instrument SNAP at the Spallation Neutron Source (SNS), Oak Ridge National Laboratory (ORNL), we have extended such measurements to pressures exceeding 50 GPa. Using this capability, we have made direct observations of the location of the deuterons under these conditions.

Results

We collected room temperature data from five independent samples of D_2O, each loaded into S-DACs (*Materials and Methods*). The resulting powder data for samples 1–3 were fitted by Rietveld-refinement (26) using the conventional structure of ice VII (19, 24, 27) (Fig. 1*A*). A "single-site" model was used for the O atoms (19, 24, 27), which were fixed on the high-symmetry bcc lattice sites, while the deuterium atoms were distributed over tetrahedral sites about these (see *Materials and Methods* for details of refinements). Hereafter, this is referred to as the "conventional" model.

Inspection of intensity as a function of angle indicated good-quality (*Materials and Methods*) powders of ice were formed. And up to ∼26 GPa, Rietveld refinements of all long data collections (samples 1–3) yielded low crystallographic R-factors (see Fig. 2*A*), indicating good fits to the conventional model. Moreover, our structural parameters agree well with previously published refinements where the data overlap in pressure (19, 24, 27). However, above ∼26 GPa, we observed a consistent and significant reduction in the quality of the fits to all datasets for the conventional model (Figs. 1*A* and 2*A*). In this pressure range, no new peaks are observed, nor do any peaks disappear, implying no change in symmetry, but specific misfits between observed and calculated intensities are common to all five samples (three are shown in Fig. 1*A*), and these could not be described within the available parameters of the conventional model.

One of the most prominent observed misfits is the increase in intensity of the 220 reflection relative to the 110 reflection. To investigate this further, sample 4 was used to track the ratio of the intensity of the 220 and 110 Bragg peaks, $\mathfrak{R}$. The relatively strong intensity of these reflections meant that the ratio was determined with sufficient precision with short collection times (∼1 h) and its pressure behavior could be sampled with a high density of points. The results (Fig. 2*B*) indicate a clear change in behavior at ∼13 GPa. After initially decreasing with pressure, $\mathfrak{R}$ is seen to increase linearly. Samples 1–3 were all consistent with

Author contributions: M.G. designed research; M.G., C.A.T., J.J.M., A.M.d.S., and K.L. performed research; M.G., R.B., J.J.M., and A.M.d.S. contributed new reagents/analytic tools; M.G. analyzed data; and M.G., R.B., C.A.T., and R.J.H. wrote the paper.

The authors declare no conflict of interest.

[1]To whom correspondence may be addressed. E-mail: mguthrie@ciw.edu or hemley@gl.ciw.edu.

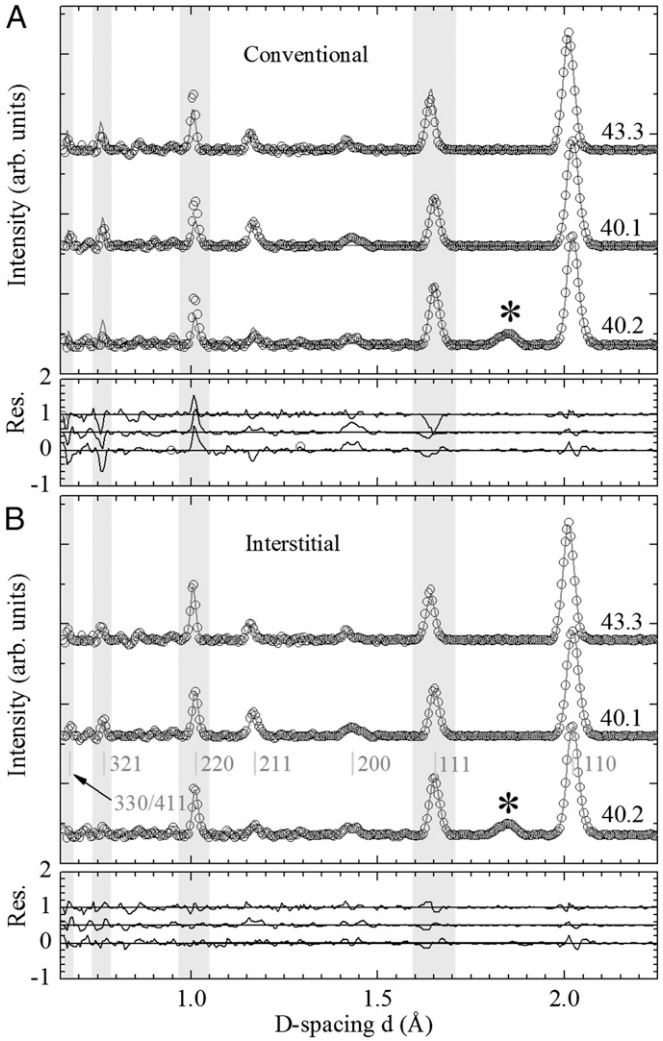

Fig. 1. Neutron diffraction patterns and Rietveld refinements of samples 1–3 at their highest pressures. *A* and *B* each contain two panels showing all three datasets. *Upper* panels show the data as open circles (samples 1–3 are shown from bottom to top); the Rietveld fit as a solid line passing through these and sample pressure in GPa is given on the right. The asterisk marks a contaminant peak from the steel gasket that was present in sample 1. The lower panels show the fit residuals in the same order as the data. *A* shows fits with conventional model, while *B* shows the fits with the interstitial model. Lightly shaded vertical bands highlight the diffraction peaks that exhibit the most prominent misfits of the conventional structure and which contrast with the much greater quality of fit for the interstitial model. Also shown in *B* are the positions and indices of the seven strongest peaks in the ice VII diffraction pattern. The refinements were carried out using GSAS (26).

this, confirming ~13 GPa to be a turning point for $\mathfrak{R}$. Finally, sample 5 was prepared with a smaller sample size and was used to extend the measurement of $\mathfrak{R}$ up to 52 GPa, indicating that the linear increase in $\mathfrak{R}$ continues up to at least this pressure.

In addition to upstroke data collection, $\mathfrak{R}$ was also measured upon downloading sample 4 and demonstrated complete reversibility (a slight increase in $\mathfrak{R}$ of around 1 standard deviation at the lowest download points is consistent with an increase in attenuating path length through the gasket due to its permanent, plastic deformation). That $\mathfrak{R}$ recovers as pressure is removed is important as it allows discounting the artifact of preferred orientation as a possible explanation of the variation of $\mathfrak{R}$: on downstroke there is no reversal of forces that could cause crystallites to "redisorder" their orientations in this way.

The 13 GPa turnover of $\mathfrak{R}$ is intriguing as it corresponds to many reported anomalies in both ices VII and VIII. Besson et al. (28) observed a roughly parabolic behavior of the υ_1 vibron line width in D_2O ices VII and VIII with a clear minimum at ~13 GPa, implying increased disorder above this pressure. Meanwhile, measurements of the VII–VIII transition temperature by Pruzan et al. (29, 30) show that this begins to decrease markedly between 10 and 18 GPa (being constant below this pressure). Yoshimura et al. (22) reported a low-frequency, Raman peak in H_2O ice VIII at 14 GPa and linked this to an anomaly in c/a ratio measured with X-ray diffraction at a similar pressure. Finally, radial X-ray diffraction measurements of H_2O ice VII by Somayazulu et al. (21) indicate a change in bulk elastic properties at 14 GPa, and splitting of diffraction lines was also reported.

With extensive evidence for an anomaly at ~13 GPa from these other studies, and being able to discount preferred orientation as an explanation for our intensities, we proceeded to investigate possible structural explanations for our observations.

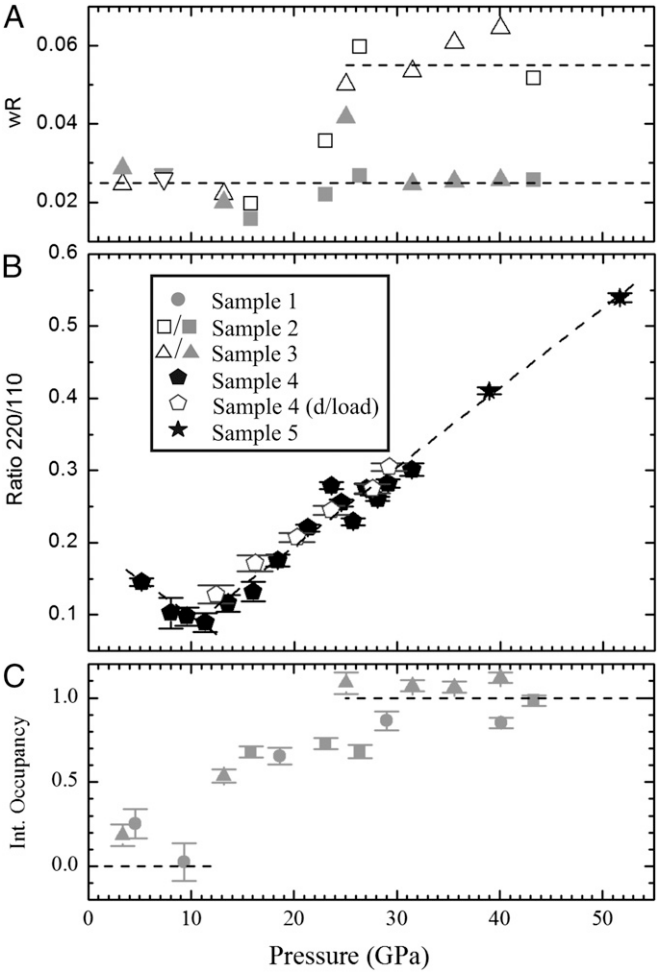

Fig. 2. Results of the neutron diffraction structure refinement. *A* shows the weighted crystallographic R-factor (wR) indicating quality of fit for samples 2 (squares) and 3 (upward triangles) for the conventional (open symbols) and interstitial (solid symbols) models (nb the steel contamination distorted wR for sample 1, which isn't shown, although the interstitial model was also strongly favored at high pressure). *B* shows the ratio $\mathfrak{R}$ described in the text, measured for samples 4 (pentagons) and 5 (stars); solid symbols were collected on upstroke and open symbols on downstroke. *C* shows the refined deuteron occupancy for the interstitial model (given as average number of D atoms per unit cell) as a function of pressure for samples 1–3. Dashed lines are guides to the eye in all panels.

PHYSICS

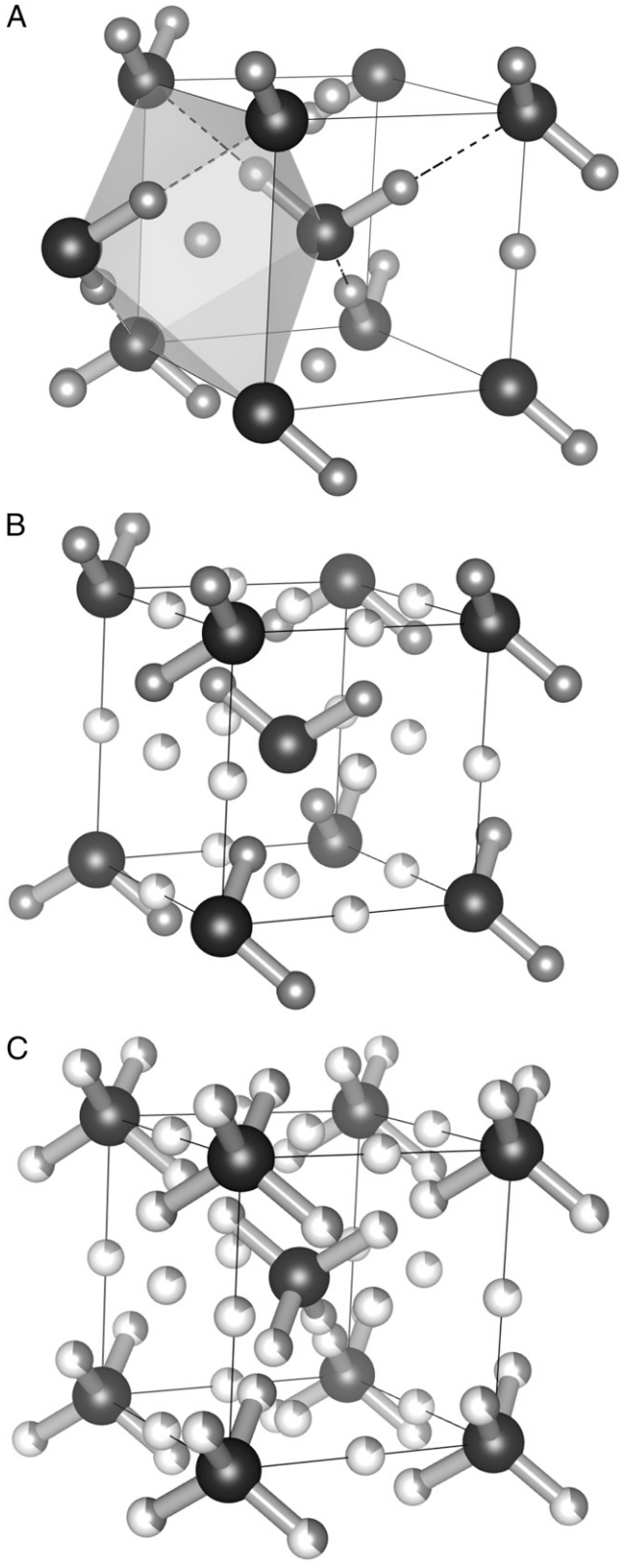

Fig. 3. Structural model for ice VII with interstitial deuterons (protons) obtained from the neutron diffraction refinement. Oxygen atoms and deuterons (protons) are shown as large and small spheres, respectively. *A* shows a rendition of a possible local fragment of the interstitial model with the octahedral void shaded. *B* shows a possible arrangement of the conventional ice VII model with all possible interstitial sites indicated as white spheres with a shaded segment indicating partial occupancy. *C* shows the full temporally and spatially averaged structure that is probed by the diffraction intensities and is refined in the interstitial model highlighting the effect of averaging. The representations of the structure were generated with VESTA (39).

As the basic oxygen framework is well established from X-ray diffraction measurements, we focused on modifications associated with the deuterons. First, we considered a "centered" model for the deuteron density distribution that might be expected at the onset of symmetrization. Here, the D atoms were placed at the midpoint of the two H-bonded O atoms (*Materials and Methods*) and given anisotropic atomic displacement parameters (describing a "cigar-like" density distribution parallel to the O...O contact). This model is appropriate for scenarios where protons are able to tunnel readily between neighboring potential minima, leading to an ellipsoidal average distribution that is symmetric about the bond midpoint. However, this model gave a negligible improvement to fit.

In a second model, we placed D atoms on the four alternative tetrahedral sites about the O atoms (*Materials and Methods*) that would indicate the formation of new H-bonds linking the two interpenetrating H-bond networks that are not bonded in the conventional structure. The occupancy of these "internetwork" sites was allowed to refine with the stoichiometry constrained. However, these refinements consistently yielded negligible or even negative occupancies for the internetwork sites, indicating the data do not support this model.

A third model investigated was one reflecting the recent proposal of a "plastic" ice (18) VII phase, where the centers-of-mass of the molecules are fixed on the bcc crystal lattice but the molecular orientation is completely disordered. In diffraction, where the temporally and spatially averaged structure is measured, these molecules would appear as large spherically symmetric species (with radii close to the O–D bond length) centered on the oxygen sites. The resultant structure has a higher symmetry than that of the conventional model, leading to the complete loss of intensity in certain reflections such as the 111. Correspondingly, we could exclude this model as the 111 remains a strong reflection in all of our datasets at all pressures (Fig. 1).

Given the failures of the models above to fit the experimental data, we focused more closely the observed strengthening of the 220 reflection. This suggested that we should examine possible structures with increased nuclear scattering density in the 220 crystal plane. An interesting way that this can be achieved is to occupy the sites that correspond to the octahedral interstitial spaces in the O lattice. As this effect is not seen with X-ray diffraction, these new scattering centers must originate from the deuterons. Correspondingly, we created a model structure with a deuteron on the interstitial site, allowing its occupancy to vary with the overall stoichiometry constrained. As the location of the interstitial site is fixed due to symmetry, its occupancy is the only additional refinement parameter required relative to the conventional model (*Materials and Methods*).

When we refined this interstitial model, we found dramatic improvements in the quality of fit across the entire pressure range of our refinable datasets (samples 1–3) up to 43 GPa. The model accounted for the intensities of all observed peaks (Fig. 1*B*), and the resulting crystallographic R-factor was as good as for the low-pressure conventional model across the full-pressure range of our datasets (Fig. 2*A*). Above the pressure where the conventional model fails, the R-factor for the interstitial model is lower by a full factor of two, which is highly significant, given that only a single additional parameter is required.

Quantitative analysis of the interstitial deuteron density reveals that above ~13 GPa, where we observe the change in the pressure dependence of $\mathfrak{R}$, the interstitial model yields a consistently nonzero interstitial site occupancy (Fig. 2*C*). This appears to reach a plateau around 30 GPa, giving on average one interstitial

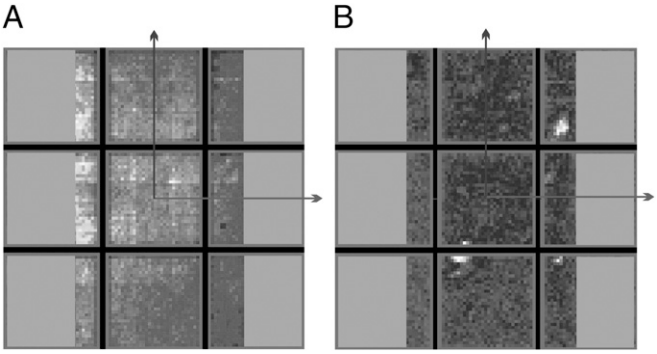

Fig. 4. Images of one of the detector banks for the highest pressure dataset from sample 2 (*A*) and for a separate measurement of a sample of deuterated ammonia-IV (*B*) in a very similar pressure cell. Each panel shows the nine modules that comprise a detector that are each divided into much smaller pixels. The shading scale represents the total neutron counts (increasing from dark to light) in each pixel integrated over a fixed range of d-spacings. The vertical axes correspond to the vertical axis of the instrument and the horizontal axes points along the beam (with scattering angle 2θ increasing from right to left). Greyed out areas correspond to where the cell aperture truncates the diffracted signal; these are also excluded when generating the powder diffraction patterns. The intensities are shown at a fixed d-spacing and thus correspond to a range of wavelengths that increase with 2θ. In *A*, the d-spacing range is centered on the ice VII 110 peak; in *B*, it is centered on the 111 and 021 reflections of ammonia-IV. D-space slices such as these are extremely useful for assessing powder quality; it is clearly seen that the ammonia sample in *B* is a poor powder, with large crystallites, while the D_2O sample in *A* (which is typical of all our ice VII samples) is highly uniform.

deuteron for every two water molecules. The diffraction measurement is sensitive to structure that is spatially averaged over the illuminated sample volume (~0.05 mm^3) and temporally averaged over the time of the measurement (5–6 h for samples 1–3). Thus, we cannot resolve between possible local scenarios for the formation of interstitial deuteron species (such as $D_2O \rightarrow D^+ + DO^-$ or $D_2O \rightarrow D_2 + O$) nor identify the local interaction of the remaining O atoms and molecular dipoles to these species (Fig. 3). However, our quantification of the average amount of deuteron density in the interstitial voids is robust.

Discussion

The difference between the interstitial model and most previous pictures of dense ice is striking. To date, it has been assumed that the protons (or deuterons) in ice remain localized close to the line joining two H-bonded oxygen atoms deep into the symmetric phase. In contrast, the interstitial model shows surprising structural similarities with metal hydrides despite the hydrogen in this case existing as an anion. Indeed, the calculated potential experienced by a proton in a bcc array of metal ions has a shallow minimum on these same octahedral sites (31). And these sites are seen to become occupied in VH_2 at low temperatures (32), with an accompanying tetragonal distortion of the bcc cell. In the case of ice, the O–D covalent bond is rather strong. However, it is possible that the H-bond itself continually strengthens as pressure increases, which counteracts the O–D covalency and provides a mechanism for dissociation. It is also possible to speculate that dissociation may be triggered by Bjerrum-type defects, which are common to all disordered phases of ice (1). Once the deuteron escapes from the molecule, this will likely have a weakening effect on the network. This could explain the anomalies in strength found in radial X-ray diffraction experiments (21) and may be related to the appearance of a new low-frequency mode in the Raman signal in ice VIII (22).

Previous theoretical work on ice VII (see refs, 15, 16, 20 and references therein) indicates that the conventional structure is the stable form, but our neutron data contrast with this and suggest an alternative picture. There are several possible explanations for this discrepancy: one is that the intrinsically dynamic, disordered structure of ice VII makes it difficult to model in a conventional ab initio approach. The small simulation sizes enforced by constraints on computational power may not be able to capture any intermediate range correlations in the structure. And techniques to circumnavigate this limitation [such as the graph invariant approach (33)] presuppose a fixed molecular structure. Another possibility is that the highly quantum nature of the proton/deuteron may not be adequately treated. Finally, the simplest explanation is that interest has tended to focus on the much higher pressure regime (approaching 100 GPa), where understanding symmetrization of the conventional H-bonds has been the driving motivation. Whichever the explanation, the differences between the interstitial structure and previous theoretical models are prominent and may hint at important physics.

In conclusion, our neutron diffraction measurements reveal a mechanism for pressure-induced dissociation of D_2O (and by inference H_2O) with a protonic species beginning to localize on the octahedral interstitial sites of the oxygen sublattice. This occurs well below the expected H-bond symmetrization transition, and distinct molecules are still present and persist in the structure. The existence of interstitial protons in ice VII has important implications for the structures of the higher pressure phases. In particular, superionicity in ice at higher *P–T* conditions has been suggested and proposed as a source of magnetic field generation in Neptune and Uranus (34–36). Protonic density on interstitial sites and potential transport via these provides a framework to model this unusual phase and could even facilitate superionicity at more modest *P–T* conditions. It is imperative to revisit existing theoretical models of ice VII to reconcile these with the current experimental observations.

Materials and Methods

Experimental Details. Four of these loadings used a design with 1.65 mm culet diamonds in strongly supported, conical tungsten carbide seats (38). An alternative design using sintered-diamond seats achieved a maximum pressure of 94 GPa with 1-mm beveled culets in testing, and the highest pressure reported here of 52 GPa was reached with 1.4 mm culet diamonds. The 250 μm thick, T301 steel gaskets were preindented to thicknesses of ~160 μm, and 650 μm holes (500 μm for the 1.4 mm culets) were drilled in these to accommodate the sample. Pressures reported here were determined using the refined unit cell volume (representing an average across the illuminated fraction, ~90% of the sample) and the H_2O Vinet equation of state reported by Somayazulu et al. (21). We note that previous neutron-diffraction data by Nelmes et al. (19) (with a refined lattice parameter of 3.047 Å) that were reported to be at 20.6 GPa based on a Murnaghan formulation of the Birch-Murnaghan equation-of-state of Hemley et al. (5) correspond to a pressure of 15.4 GPa on the scale we use.

Table 1. Fractional coordinates (*x*,*y*,*z*) for the atoms in the four models considered in the $Pn\bar{3}m$ space group, second origin setting

	O atom				First D atom				Second D atom			
Model	*x*	*y*	*z*	M	*x*	*Y*	*z*	M	*x*	*y*	*z*	M
Conventional single-site	1/4	1/4	1/4	2	x	x	x	8	Not applicable			
Internetwork	1/4	1/4	1/4	2	x	x	x	8	1/2 – x	1/2 – x	1/2 – x	8
Plastic Ice	1/4	1/4	1/4	2	1/4	1/4	1/4	2	Not applicable			
Interstitial	1/4	1/4	1/4	2	x	x	x	8	1/4	1/4	3/4	6

The column M gives the multiplicity of each site. The number of atoms in the unit cell is obtained by multiplying the average occupancy *f* with the multiplicity M of the site (e.g., in the conventional model, the occupancy of the oxygen atom f_o is 2 and that of the D atom f_D is 0.5, giving two complete water molecules per unit cell).

The incident neutron beam was focused by a parabolic mirror guide to ~2 mm diameter and then truncated by a 600 μm diameter hexagonal boron nitride collimator that contacted the back of the upstream diamond. Diffraction data from the five samples were normalized to the intensity measured from a 2 mm diameter, 1.2-mm-thick V disk held between the diamond anvils and subject to the same collimated beam incident on the sample. Diffraction peaks were clearly visible after several minutes of data collection, however, for samples 1–3, which were used for Rietveld refinement, data were collected for 5–6 h to obtain a reliable statistical determination of Bragg intensities down to d-spacings of ~0.65 Å.

To assess texture in the sample, we extracted "sheets" of constant d-spacing, centered on the strongest ice reflection (the 110 at d_{110}) across the entire active detector area. This corresponds to a projection of a spherical surface (with radius $Q_{110} = 2\pi/d_{110}$) in reciprocal space onto the flat detector. Fig. 4 shows a typical example sheet for our ice VII samples (taken from the highest pressure dataset from sample 2, for which the final diffraction pattern is shown in Fig. 1). In the figure, the high quality of the crystallite size distribution in ice VII is contrasted with an equivalent measurement of a poor powder of deuterated ammonia-IV measured in a separate experiment.

Refinement Details. All refinements were carried out in the $Pn\bar{3}m$ space group and neither new peaks nor systematic absences were observed to indicate a change in this symmetry across the pressure range spanned by our measurements. Atomic positions for each of the models considered are given in Table 1. As has been discussed in several previous studies, the local position of the oxygen atom is displaced off the special site by a small amount δ [determined to be 0.08–0.13 Å in various studies (19, 24, 27, 33)]. The direction of this displacement is contentious, and at least two distinct models (with important consequences for H-bonding) have been proposed and explored with experiment (19, 24, 27) and theory (33). The manifestation of multisite disorder in a crystallographic measurement is an enlargement of the average oxygen density distribution, and our relatively low-resolution data are not very sensitive to this. This was confirmed by a series of tests where the O atom was systematically displaced from the average site (along directions corresponding to the two main oxygen disorder models). This had an immeasurable effect on the quality of the fit, although, as expected, the refined thermal motion of the O atom correlated strongly with both the magnitude and direction of the displacement. Consequently, as described above, we use a single-site oxygen model, with the O atom on the high symmetry, average site and explicitly do not address multisite disorder of the oxygen atom in ice VII.

In addition to the positional parameters given in Table 1, an isotropic atomic displacement parameter was refined for all atoms, and for the Internetwork and Interstitial models, this was constrained to be equal for molecular and interstitial protons. In both models where the occupancy of D sites was refined, a stoichiometric constraint retaining two deuterons for each oxygen atom was used. In addition to these atomic parameters, the lattice parameters were also refined, as were standard instrumental parameters including Gaussian and Lorentzian peakshape parameters and a background function.

ACKNOWLEDGMENTS. We thank M. Somayazulu and A. Karandikar for experimental assistance and H. K. Mao, A. F. Goncharov, R. E. Cohen, R. Von Dreele, and B. H. Toby for discussions. This work is supported by EFree, an Energy Frontier Research Center funded by the US Department of Energy (DOE), Office of Science, Office of Basic Energy Sciences (BES) under Award DE-SC0001057. Research conducted at the Spallation Neutron Source (SNS) was supported by the Scientific User Facilities division, BES, DOE, under Contract DE-AC05-00OR22725 with UT-Battelle, LLC.

1. Petrenko VF, Whitworth RW (2002) *Physics of Ice* (Oxford Univ Press, Oxford, UK).
2. Goncharov AF, Struzhkin VV, Somayazulu M, Hemley RJ, Mao HK (1996) Compression of ice to 210 GPa: Evidence for a symmetric hydrogen bonded phase. *Science* 273(5272): 218–220.
3. Aoki K, Yamawaki H, Sakashita M, Fujihisa H (1996) Infrared absorption study of the hydrogen-bond symmetrization in ice to 110 GPa. *Phys Rev B Condens Matter* 54(22): 15673–15677.
4. Struzhkin VV, Goncharov AF, Hemley RJ, Mao HK (1997) Cascading Fermi resonances and the soft mode in dense ice. *Phys Rev Lett* 78(23):4446–4449.
5. Hemley RJ, et al. (1987) Static compression of H_2O-ice to 128 GPa (1.28 Mbar). *Nature* 330:737–740.
6. Wolanin E, et al. (1997) Equation of state of ice VII up to 106 GPa. *Phys Rev B* 56(10): 5781–5785.
7. Sugimura E, et al. (2008) Compression of H_2O ice to 126 GPa and implications for hydrogen-bond symmetrization: Synchrotron x-ray diffraction measurements and density-functional calculations. *Phys Rev B* 77(21):214103.
8. Loubeyre P, LeToullec R, Wolanin E, Hanfland M, Häusermann D (1999) Modulated phases and proton centering in ice observed by X-ray diffraction up to 170 GPa. *Nature* 397:503–506.
9. Hemley RJ, Dera P (2000) *High-Temperature and High-Pressure Crystal Chemistry*, eds Hazen RM, Downs RT (MSA, Washington, DC), Vol 41, pp 335–419.
10. Song M, Yamawaki H, Fujihisa H, Sakashita M, Aoki K (1999) Infrared absorption study of fermi resonance and hydrogen-bond symmetrization of ice up to 141 GPa. *Phys Rev B* 60:12644–12650.
11. Goncharov AF, Struzhkin VV, Mao HK, Hemley RJ (1999) Raman spectroscopy of dense H_2O and the transition to symmetric hydrogen bonds. *Phys Rev Lett* 83(10): 1998–2001.
12. Ahart M, et al. (2011) Brillouin scattering of H2O ice to megabar pressures. *J Chem Phys* 134(12):124517.
13. Zha CS, Hemley RJ, Gramsch SA, Mao HK, Bassett WA (2007) Optical study of H_2O ice to 120 GPa: Dielectric function, molecular polarizability, and equation of state. *J Chem Phys* 126(7):074506.
14. Benoit M, Marx D, Parrinello M (1998) Tunneling and zero-point motion in high-pressure ice. *Nature* 392:258–261.
15. Caracas R (2008) Dynamical instabilities of ice X. *Phys Rev Lett* 101(8):085502.
16. Schwegler E, Galli G, Gygi F (2000) Water under pressure. *Phys Rev Lett* 84(11): 2429–2432.
17. Hermann A, Ashcroft NW, Hoffmann R (2012) High pressure ices. *Proc Natl Acad Sci USA* 109(3):745–750.
18. Takii Y, Koga K, Tanaka H (2008) A plastic phase of water from computer simulation. *J Chem Phys* 128(20):204501.
19. Nelmes RJ, et al. (1998) Multisite disordered structure of ice VII to 20 GPa. *Phys Rev Lett* 81(13):2719–2722.
20. Benoit M, Romero AH, Marx D (2002) Reassigning hydrogen-bond centering in dense ice. *Phys Rev Lett* 89(14):145501.
21. Somayazulu M, et al. (2008) In situ high-pressure x-ray diffraction study of H_2O ice VII. *J Chem Phys* 128(6):064510.
22. Yoshimura Y, Stewart ST, Somayazulu M, Mao HK, Hemley RJ (2006) High-pressure x-ray diffraction and Raman spectroscopy of ice VIII. *J Chem Phys* 124(2):024502.
23. Polian A, Grimsditch M (1984) New high-pressure phase of H_2O: Ice X. *Phys Rev Lett* 52(15):1312–1314.
24. Kuhs WF, Finney JL, Vettier C, Bliss DV (1984) Structure and hydrogen ordering in ices VI, VII, and VIII by neutron powder diffraction. *J Chem Phys* 81(8):3612–3623.
25. Kamb BYB, Davis BL (1964) Ice VII, the densest form of ice. *Proc Natl Acad Sci USA* 52(6):1433–1439.
26. Larson AC, Dreele RV (2000) General Structure Analysis System (GSAS). *Los Alamos National Laboratory Report* 86–748.
27. Jorgensen JD, Worlton TG (1985) Disordered structure of D_2O ice VII from in situ neutron powder diffraction. *J Chem Phys* 83(1):329–333.
28. Besson JM, Kobayashi M, Nakai T, Endo S, Pruzan P (1997) Pressure dependence of Raman linewidths in ices VII and VIII. *Phys Rev B* 55(17):11191–11201.
29. Pruzan P, Chervin JC, Canny B (1992) Determination of the D_2O ice Vii-Viii transition line by Raman-scattering up to 51 GPa. *J Chem Phys* 97(1):718–721.
30. Pruzan P, Chervin JC, Canny B (1993) Stability domain of the ice-VIII proton-ordered phase at very high-pressure and low-temperature. *J Chem Phys* 99(12):9842–9846.
31. Murray JS, Sen KD, eds (1996) *Molecular Electrostatic Potentials - Concepts and Applications* (Amsterdam, The Netherlands).
32. Asano H, Hirabayashi M (1973) Interstitial superstructures of vanadium deuterides. *Phys Status Solidi* 15(1):267–279.
33. Knight C, Singer SJ (2009) Site disorder in ice VII arising from hydrogen bond fluctuations. *J Phys Chem A* 113(45):12433–12438.
34. Goncharov AF, et al. (2005) Dynamic ionization of water under extreme conditions. *Phys Rev Lett* 94(12):125508.
35. Cavazzoni C, et al. (1999) Superionic and metallic states of water and ammonia at giant planet conditions. *Science* 283(5398):44–46.
36. Schwegler E, Sharma M, Gygi F, Galli G (2008) Melting of ice under pressure. *Proc Natl Acad Sci USA* 105(39):14779–14783.
37. Momma K, Izumi F (2011) VESTA 3 for three-dimensional visualization of crystal, volumetric and morphology data. *J Appl Cryst* 44(6):1272–1276.
38. Boehler R, DeHantsetters K (2004) New designs in diamond anvils. *High Pressure Research* 24(3):391–396.